Supplementary Materials: Reconfigurable Integrated Photonic Processor for NP-complete Problems

Xiao-Yun Xu[a,b,d], **Tian-Yu Zhang**[a,b], **Zi-Wei Wang**[a,b], **Chu-Han Wang**[a,b], **Xian-Min Jin**[a,b,c,d,*]
[a]Center for Integrated Quantum Information Technologies (IQIT), School of Physics and Astronomy and State Key Laboratory of Advanced Optical Communication Systems and Networks, Shanghai Jiao Tong University, Shanghai 200240, China.
[b]Hefei National Laboratory, Hefei 230088, China.
[c]TuringQ Co., Ltd., Shanghai 200240, China.
[d]Chip Hub for Integrated Photonics Xplore (CHIPX), Shanghai Jiao Tong University, Wuxi 214000, China.

Contents

1 Splitting ratio of variable split junctions

As depicted in Fig. 1(d), the variable split junctions are implemented with 3D Mach-Zender interferometers (MZIs) composed of two modified 50:50 directional couplers (DCs) and a phase shifter (PS), which can be represented by the matrix

$$\begin{aligned} U_{MZI} &= \frac{1}{\sqrt{2}} \begin{pmatrix} 1 & i \\ i & 1 \end{pmatrix} \begin{pmatrix} e^{i\varphi_t/2} & 0 \\ 0 & e^{-i\varphi_t/2} \end{pmatrix} \frac{1}{\sqrt{2}} \begin{pmatrix} 1 & i \\ i & 1 \end{pmatrix} \\ &= -i \begin{pmatrix} \sin\frac{\varphi_t}{2} & \cos\frac{\varphi_t}{2} \\ \cos\frac{\varphi_t}{2} & -\sin\frac{\varphi_t}{2} \end{pmatrix}, \end{aligned} \tag{S1}$$

where φ_t is the total phase difference between the two interferometer arms. Note that $\varphi_t = \varphi + \varphi_0$, where φ is induced by the phase shifter and φ_0 is the original phase difference arising from imperfect fabrication. According to equation (S1), the MZIs have a reflectivity $\eta = \sin^2\frac{\varphi_t}{2} = \frac{1-\cos\varphi_t}{2}$, which is dependent on the phase difference φ_t. With an appropriate setting of the applied current of the phase shifter, η can vary from 0 to 1, indicating that the variable split junctions enable arbitrary specified splitting ratio $\eta : 1-\eta$.

2 Structure of the functional modules

Four different kinds of functional modules are arranged according to particular rules to form the waveguide network enabling to solve the SSP, as introduced in the main text. Fig. S1(a) shows an overview of the top corner of the waveguide network, from which we can see the actual layout of the functional modules. Light is injected through the network entries located at the front end of the photonic processor, as denoted by red arrows. The spacing between a blue waveguide and its

next nearest cyan waveguide is 30 μm, which is also the y-direction distance between two neighboring variable (or fixed) split junctions. At this distance, the energy exchange through evanescent coupling is negligible as presented in Supplementary Section 3. Phase shifters in the variable split junctions (encircled by green dashed lines) are spaced along x direction. The separation between the upper and the lower phase shifters is 5 mm, which is large enough to eliminate the thermal crosstalk between them (see Supplementary Section 9). More details on the physical structure of the functional modules are depicted by the sketches in Figs. S1(b)-S1(e). Noted that, in order to clearly show the structure design, different parts of the functional modules are displayed in different scales.

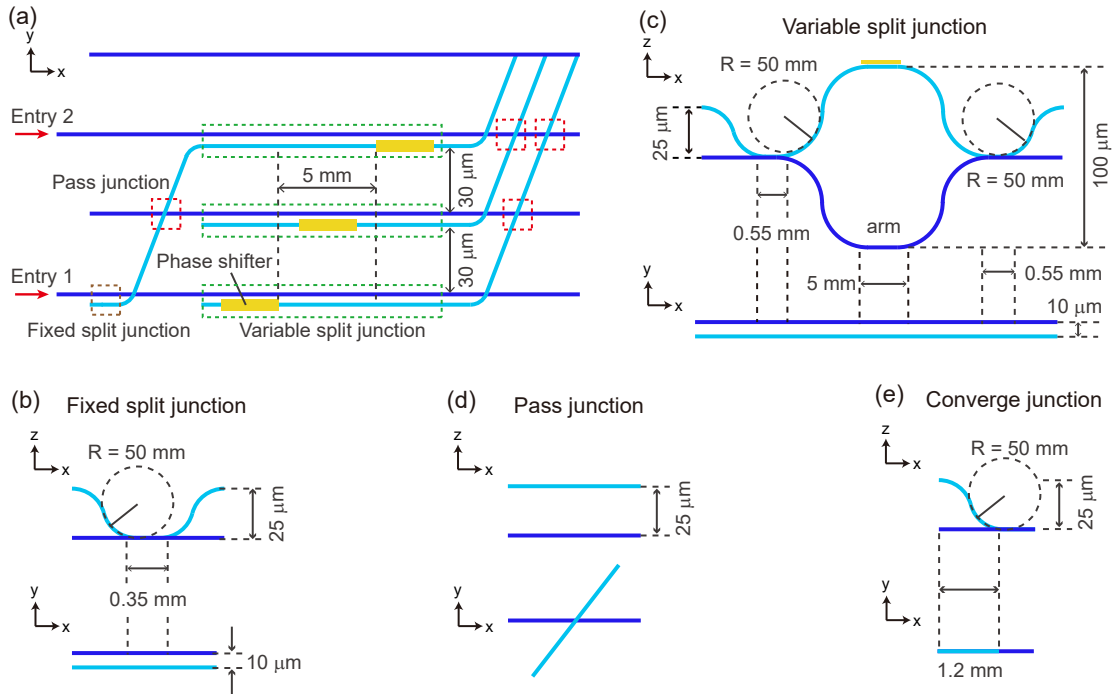

Fig S1 An overview of the top corner of the waveguide network, and the functional modules. (**a**) The x-y view of the top corner of the waveguide network, which constitutes standardized functional modules, fixed split junctions (brown lines), variable split junctions (green lines) and pass junctions (red lines). (**b**)-(**e**) Sketches of fixed split junctions, variable split junctions, pass junctions and converge junctions.

Fixed split junctions (encircled by brown dashed lines in Fig. S1(a)) are actually modified three-dimensional directional couplers which have a bending radius of 50 mm, as displayed in Fig.

S1(b). A coupling length of 0.35 mm and a coupling distance of 10 μm are utilized to achieve a balanced splitting ratio (see Supplementary Section 3). Also, the z-direction spacing between the two input (or output) ports is deliberately set to 25 μm to realize decoupling (see Supplementary Section 3).

Variable split junctions (encircled by green dashed lines in Fig. S1(a)) are realized by Mach-Zehnder interferometers made of two cascaded three-dimensional 50:50 directional couplers, as depicted in Fig. S1(c). The directional couplers are the mirror image of each other and they are connected by the interferometer arms with a length of 5 mm. A bending radius of 50 mm, a coupling length of 0.55 mm and a coupling distance of 10 μm are used to achieve a balanced splitting ratio. Compared with fixed split junctions, the z-direction spacing between the two outputs of the first coupler (or between the two inputs of the second coupler) is increased to 100 μm to enhance the temperature difference between the interferometer arms.

Pass junctions (encircled by red dashed lines in Fig. S1(a) is composed of two completely separate waveguides. As exhibited in Fig. S1(d), the waveguides look like intersecting with each other in the x-y view, but they are actually written at different depths of the photonic processor as displayed in the x-z view. The distance between them in z direction is 25 μm, which allows to decoupling the two waveguides.

Converge junctions are located at the back end of the whole waveguide network, which are not depicted in Fig. S1(a). The two waveguides in converge junctions are separated at the beginning but finally merge into one whole (see Fig. S1(e)), which is designed to gather together photons from different paths.

3 Optimization of the photonic processor

The computing accuracy and reliability of the photonic processor are dependent on the performances of the functional modules or even the quality of the waveguides. Here, we optimize the photonic processor by elaborately selecting the spacing between two decoupled waveguides and the coupling length of fixed and variable split junctions.

The decoupling distance is chosen based on the model that consists of two parallel straight waveguides. One of the waveguides acts as the input where a 808 nm laser (Fiblaser FCM808S40UC1P0) is injected. The other waveguide usually stretches from the middle of the input waveguide to the same ending position to the input waveguide, resulting in a shorter length of L. In addition, the two waveguides has a spacing of D. For decoupled waveguides, there is no energy exchange between them (or there is no transmission from the input waveguide to the other) regardless of the increase of L. Accordingly, we have fabricated several groups of the two-waveguide models, where spacing D is gradually increased. In each group, spacing D is fixed and there are several two-waveguide models where length L is increased.

Fig. S2(a) presents the experimental results when the *y*-direction waveguide spacing D is 30 μm. We can clearly see that the output signal always stays in the input waveguide (the other waveguide is marked by white dashed lines), though the waveguide length L varies at a large range (from 45 mm to 95 mm). The intensity distribution remains unchanged despite the increase of waveguide length and the intensity ratio between the two outputs is up to several hundred. The phenomenon reveals that the evanescent coupling between the waveguides is negligible. Therefore, 30 μm is used as the *y*-direction decoupling distance. Similar results are obtained when the *z*-direction waveguide spacing D is 25 μm (Fig. S2(b)). As a result, 25 μm is used as the *z*-direction

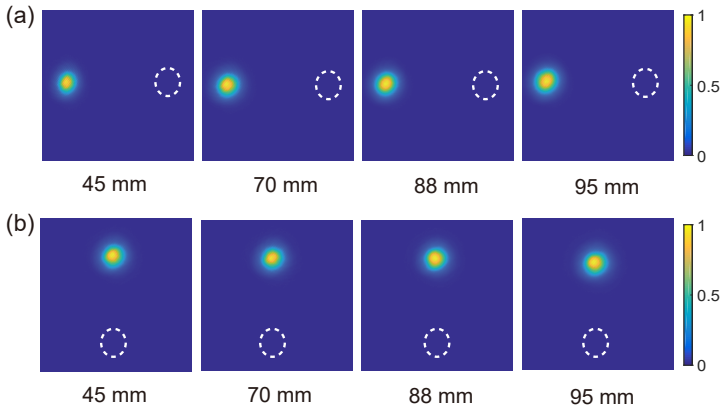

Fig S2 Experimental intensity distribution of two decoupled waveguides. (**a**) The waveguides are separated in y direction at a constant distance of 30 μm, whereas the waveguide length L varies from 45 mm to 95 mm. A 808 nm laser is coupled into the left waveguide. The position of the right waveguide is marked by dashed lines. (**b**) The waveguides are separated in z direction at a constant distance of 25 μm while the waveguide length L varies from 45 mm to 95 mm. A 808 nm laser is coupled into the upper waveguide. The position of the lower waveguide is marked by dashed lines.

decoupling distance. The difference between the decoupling distance in the y and z directions is attributed to the direction-dependent coupling coefficient of the waveguides.

Based on the decoupling distance, we continue to optimize the coupling length of fixed and variable split junctions. Given that coupling distance and coupling length play a similar role in evanescent coupling, we fix the coupling distance to 10 μm while increase the coupling length at a step of 0.1 mm. For fixed split junctions, a coupling length of 0.3 mm (0.4 mm) leads to a splitting ratio of 53:47 (47:53), which is slightly higher (lower) than 50:50 as shown in Fig. S3(a). In theory, the splitting ratio varies smoothly in a manner of cosine oscillation with the increase of coupling length. Therefore, a coupling length of 0.35 mm is adopted to approximately achieve a balanced splitting ratio. For variable split junctions, we are concerned about the splitting ratio of the cascaded directional couplers. As exhibited in Fig. S3(b), the coupling length 0.5 mm (0.6 mm) leads to a splitting ratio of 53:47 (49:51), which is slightly higher (lower) than 50:50. Similar to the previous case, a coupling length of 0.55 mm is applied to the directional couplers.

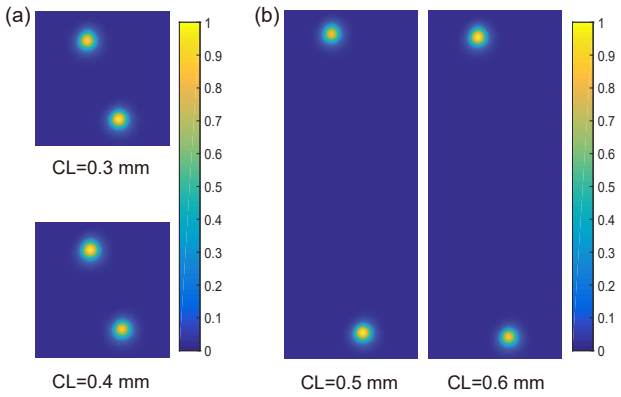

Fig S3 Experimental intensity distribution of fixed and variable split junctions. (**a**) The intensity distribution of fixed split junctions when the coupling length (CL) is 0.3 mm and 0.4 mm, respectively. (**b**) The intensity distribution of the directional coupler in variable split junctions when the coupling length (CL) is 0.5 mm and 0.6 mm, respectively.

4 Experimental setup

As presented in Fig. S4, the photonic processor, with phase shifters deposited on the surface, is bonding to a printed circuit board (PCB). The PCB connects to an external power supply to control the dissipated power of the phase shifters, with the assistance of a flexible printed circuit (FPC) and a second PCB. The power supply is set to constant current mode to eliminate the electrical crosstalk between the phase shifters. A single-mode 808 nm laser (Fiblaser FCM808S40UC1P0) is coupled into the photonic processor through an objective (OBJ). The output light are focused by two lenses and collected by a charge-coupled device (CCD). Note that the packaged photonic processor and the objective are mounted to high-dimensional precision translational stages to ensure accurate optical alignment. Both the characterization of variable split junctions and the computation of the SSP are carried out with the setup.

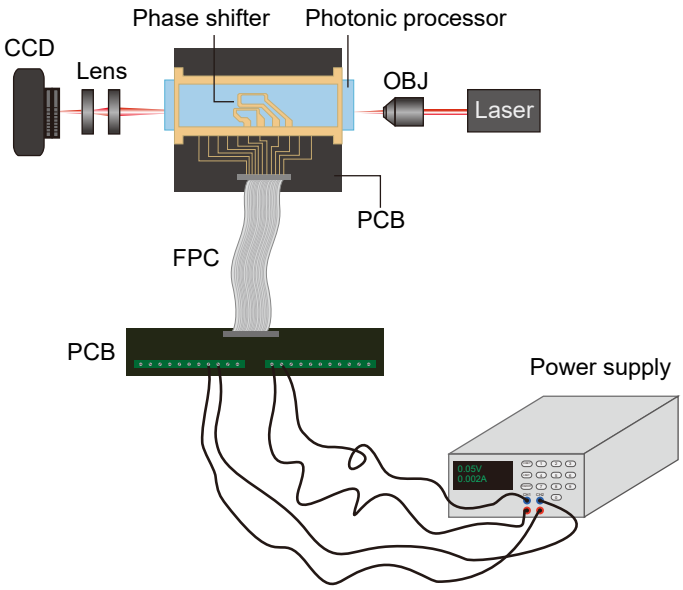

Fig S4 Experimental setup. CCD: charge-coupled device; OBJ: objective; PCB: printed circuit board; FPC: flexible printed circuit.

5 Optical response of variable split junctions

(1) Characterization methods

The optical response of the variable split junctions is characterized as a function of the dissipated power P of the phase shifters. Based on Supplementary Section 1 and the linear relation between φ and P [Ref. 35], the output intensities of the variable split junctions are supposed to show cosine oscillation with the change of P. Since we cannot directly measure the output of the variable split junctions, the characterization is performed on the basis of the whole waveguide network.

Generally, a variable split junction is connected to some output ports of the waveguide network while disconnected to the others. For example, according to Fig. 1(b) in the main text, photons passing through the left variable split junction have a possibility to arrive at output port 3 (connected case) while are impossible to reach output port 2 (disconnected case). Therefore, we can obtain the optical response of the variable split junctions by monitoring the output intensity at a connected output port. Though the magnitude of the intensity at a connected port might be dif-

ferent from the output of the variable split junctions, the relative intensity changes still reflect the main properties of the optical response of the variable split junctions, enabling to identify the three working modes. The connected port used for characterization are denoted as "response port".

Since the characterization mainly relies on relative intensity changes, applying a "reference port", which reflects the environmental fluctuation, in the subsequent data processing could be beneficial to mitigate the effect of instable environment. As the crosstalk in our experiments is negligible (see Supplementary Section 9), the output intensity at disconnected port, to some extent, mirrors the environmental variations and thus can be treated as reference. During the characterization, we launched a 808 nm laser into the waveguide network through Entry 1, then gradually increased the dissipated power, P, of the phase shifter by changing the applied current, and meanwhile monitored the output of the waveguide network with a CCD. After that, we divided the intensity at the "response port" by the intensity at the "reference port" and plotted the results as a function of the dissipated power as exhibited in the next section.

(2) Experimental optical response

There are three variable split junctions in our photonic processor. According to Fig. 1(b) in the main text, the incident light, in any case, is impossible to go through the variable split junction located in the middle. Therefore, we only characterize the left and the right variable split junctions. In the case of the left variable split junction, output ports 2 and 3 serve as "reference port" and "response port", respectively. In the case of the right one, output ports 3 acts as "reference port" while output port 2 is "response port".

As shown in Fig. S5, the optical responses of both the variable split junctions show cosine oscillation, which is consistent with theoretical expectation. Meanwhile, the three kinds of working

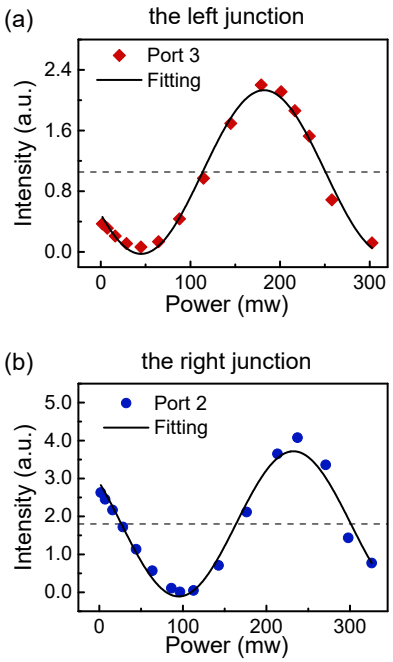

Fig S5 Experimental optical response of the variable split junctions. The optical response of the left (**a**) and the right (**b**) variable split junctions is plotted as a function of the dissipated power of the phase shifters. The experimental data are well fitted by a cosine function. The dashed lines mark the median points between the maximums and the minimums.

modes can be clearly identified. The maximums (minimums) of the response curves correspond to total reflection (transmission) mode where $\eta = 1$ ($\eta = 0$). The median points marked by dashed lines correspond to balance mode where $\eta = 0.5$. Note that the phase shifters in the left and the right variable split junctions have a resistance of 71.6 Ω and 70.5 Ω, respectively.

6 Calculation of theoretical intensity distribution

The theoretical intensity distribution is calculated based on an ideal photonic computing model where energy loss, environmental noise and fabrication imperfection are not considered. Also, all the functional modules operate in perfect conditions. It includes: (i) Fixed split junctions exactly have a splitting ratio of $0.5 : 0.5$. (ii) Variable split junctions can be perfectly switched to any of the three working modes. (iii) There is no energy exchange between the waveguides in pass junctions. (iv) In converge junctions, photons from both vertical and diagonal paths can be fully coupled into

the waveguide segment at the end of the junctions. Under the above assumption, the theoretical intensity distribution can be regarded as benchmark results.

7 Programming the photonic processor

The implemented photonic processor is able to solve more SSP instances with proper settings. (i) For the SSP instance where $S = \{2, 5, 7, 11, 13, 17\}$, the left and the right variable split junctions should be tuned to total transmission mode and total reflection mode, respectively. The working mode of the middle variable split junction makes no difference to the computing results. Meanwhile, Entry 1 is used for photon injection. (ii) With a change of the entry, we can program the photonic processor to solve the following SSP instances: $\{3, 5, 7, 11, 13, 17\}$ (Entry 2), $\{5, 7, 11, 13, 17\}$ (Entry 3), $\{7, 11, 13, 17\}$ (Entry 4), $\{11, 13, 17\}$ (Entry 5) and $\{13, 17\}$ (Entry 6). Note that, in the case of $\{3, 5, 7, 11, 13, 17\}$, the right variable split junction is switched to balance mode while the working modes of the remaining variable split junctions make no difference to the computing results. In the other cases, the working modes of all the variable split junctions have no influence on the computing results.

8 Computing results of the photonic processor

Fig. S6 presents the intensity distribution of the SSP instances where $S = \{5, 7, 11, 13, 17\}$ and $S = \{7, 11, 13, 17\}$. In both cases, the tolerance intervals of the thresholds have an upper bound that is much larger than the lower bound, as denoted by the bands filled with black solidus. Namely, there are a large range of thresholds allowing us to correctly distinguish the valid experimental signals from the invalid ones (highlighted with white solidus pattern). As introduced in the main text, an experimental signal beyond the threshold is identified to be valid certification of the corre-

sponding subset sum. In contrast, an experimental signal below the threshold is considered to be invalid.

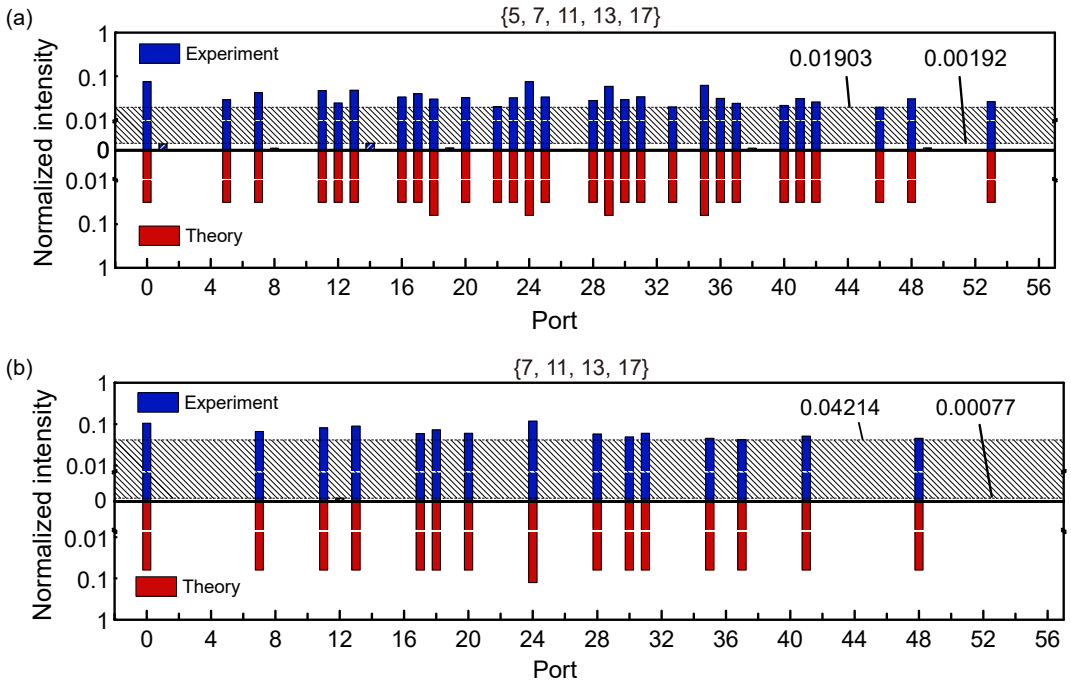

Fig S6 The intensity distribution of the cases $\{5, 7, 11, 13, 17\}$ and $\{7, 11, 13, 17\}$. (**a**) The tolerance interval of the threshold, marked by the band filled with black solidus, has an upper bound of 0.01903 and a lower bound of 0.00192 in the case of $\{5, 7, 11, 13, 17\}$. (**b**) The tolerance interval of the threshold has an upper bound of 0.04214 and a lower bound of 0.00077 in the case of $\{7, 11, 13, 17\}$, as indicated by the band filled with black solidus.

More SSP instances can be solved when photons are injected into the photonic processor through a different entry. Figs. S7(a) and S7(c) exhibit the experimental evolution results when Entry 5 and Entry 6 act as the input, respectively. It is found that the computing results agree well with the theoretical results. Also, the tolerance intervals of the thresholds, shown in Figs. S7(b) and S7(d) and marked by the bands filled with black solidus, are large enough to accept a lot of thresholds that can correctly separate the valid experimental signals from the invalid ones (highlighted with white solidus pattern).

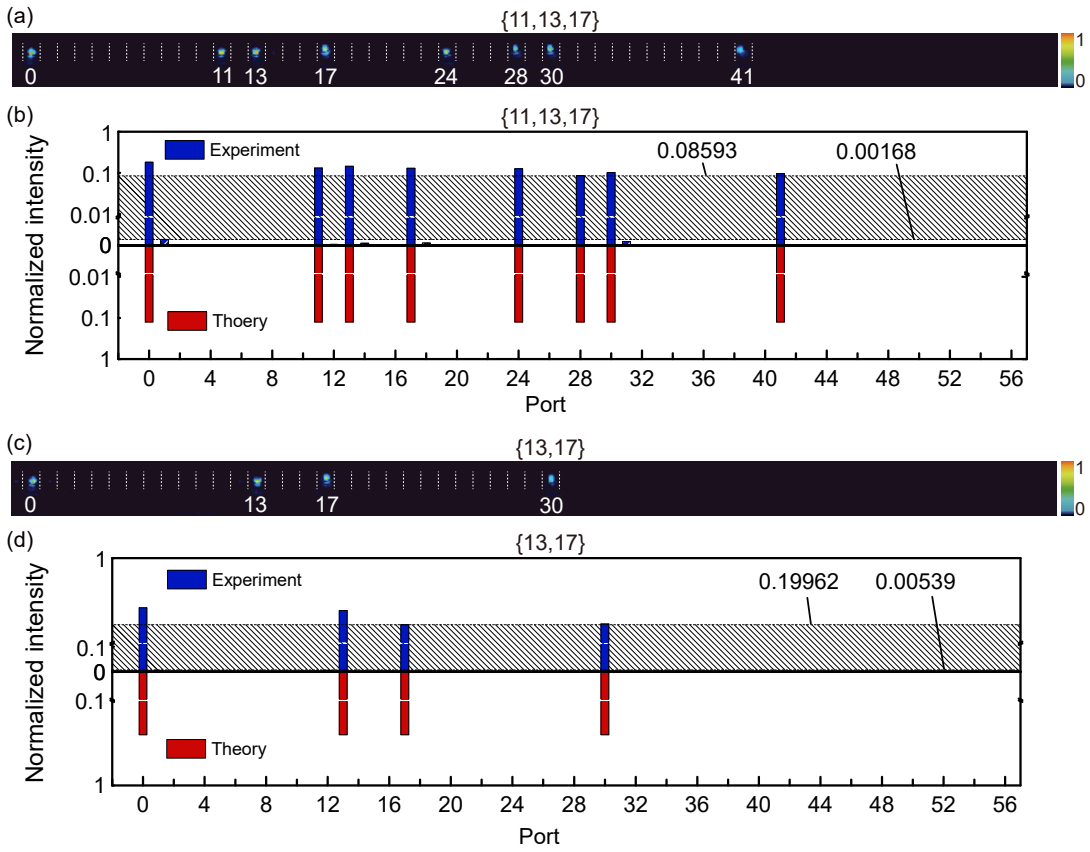

Fig S7 The computing results of the cases $\{11, 13, 17\}$ and $\{13, 17\}$. (**a**) The experimental read-out and (**b**) intensity distribution in the case of $\{11, 13, 17\}$. (**c**) The experimental read-out and (**d**) intensity distribution in the case of $\{13, 17\}$. The tolerance intervals of the thresholds are indicated by the band filled with black solidus.

9 Negligible thermal crosstalk

As the photonic processor is not a perfect thermal insulator, the phase shifter in the left variable split junction (denoted as VS junction 1) might bring an unwanted phase shift to the right variable split junction (denoted as VS junction 2) and vise versa. We can evaluate the thermal crosstalk by measuring the intensity changes at output ports that are connected to one of the VS junctions while disconnected to the other. Note that the disconnection means that there does not exist an optical path allowing photons to propagate from the variable split junction to the output ports.

The intensity at output port 2, I_2, have been monitored when we characterize the optical response of VS junction 1. During the characterization, the dissipated power of VS junction 1 grad-

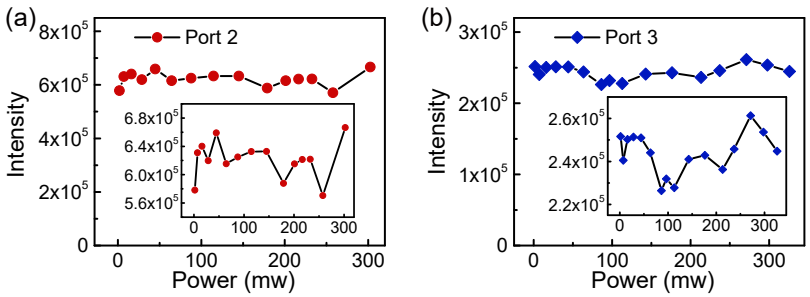

Fig S8 Intensity at output port 2 (output port 3) during the characterization of VS junction 1 (VS junction 2). (**a**) The intensity is measured when VS junction 1 is characterized and VS junction 2 undergoes a power cut. The intensity shows small irregular fluctuation, rather than cosine oscillation. (**b**) The intensity is measured when VS junction 2 is characterized and VS junction 1 undergoes a power cut. Similarly, the intensity fluctuates irregularly.

ually increases while VS junction 2 undergoes a power cut. Meanwhile, output port 2 is disconnected to VS junction 1 but connected to VS junction 2 (see Fig. 1(b) in the main text). Therefore, the intensity changes at output port 2 can be used to evaluate the thermal crosstalk. According to Supplementary Section 1 and the linear phase-power relation [Ref. 35], the increasing dissipated power of VS junction 1 can result in a cosine intensity oscillation at output port 2 if there is thermal crosstalk. However, we only observe small irregular intensity fluctuation rather than cosine oscillation as exhibited in Fig. S8(a). The fluctuation magnitude $\delta = \frac{I_2^{max} - I_2^{min}}{I_2^{max}}$ is around 14.4%, indicating the negligibility of thermal crosstalk. Moreover, the intensity variation could be attributed to environmental noise and instable incident light.

Similarly, we have also collected the intensity at output port 3, I_3, during the characterization of VS junction 2. In this case, the dissipated power of VS junction 2 gradually increases and VS junction 1 is shut down. Besides, output port 3 is disconnected to VS junction 2 while connected to VS junction 1. As presented in Fig. S8(b), the small irregular intensity fluctuation ($\sim$13.4%) at output port 3 again verifies that the thermal crosstalk is ignorable.

In addition, the negligible thermal crosstalk is further confirmed by a comparison of the computing results of the photonic processor under different conditions. We program the photonic

processor to solve the SSP instance where $S = \{3, 5, 7, 11, 13, 17\}$ by using entry 2 as the input and setting VS junction 2 to balance mode. Meanwhile, zero current is applied to VS junction 1 (i.e., the dissipated power is zero), making it impossible to introduce any thermal crosstalk. In this case, the computing results are highly reliable and coincide with theoretical results (see Figs. S9(a)-S9(b)).

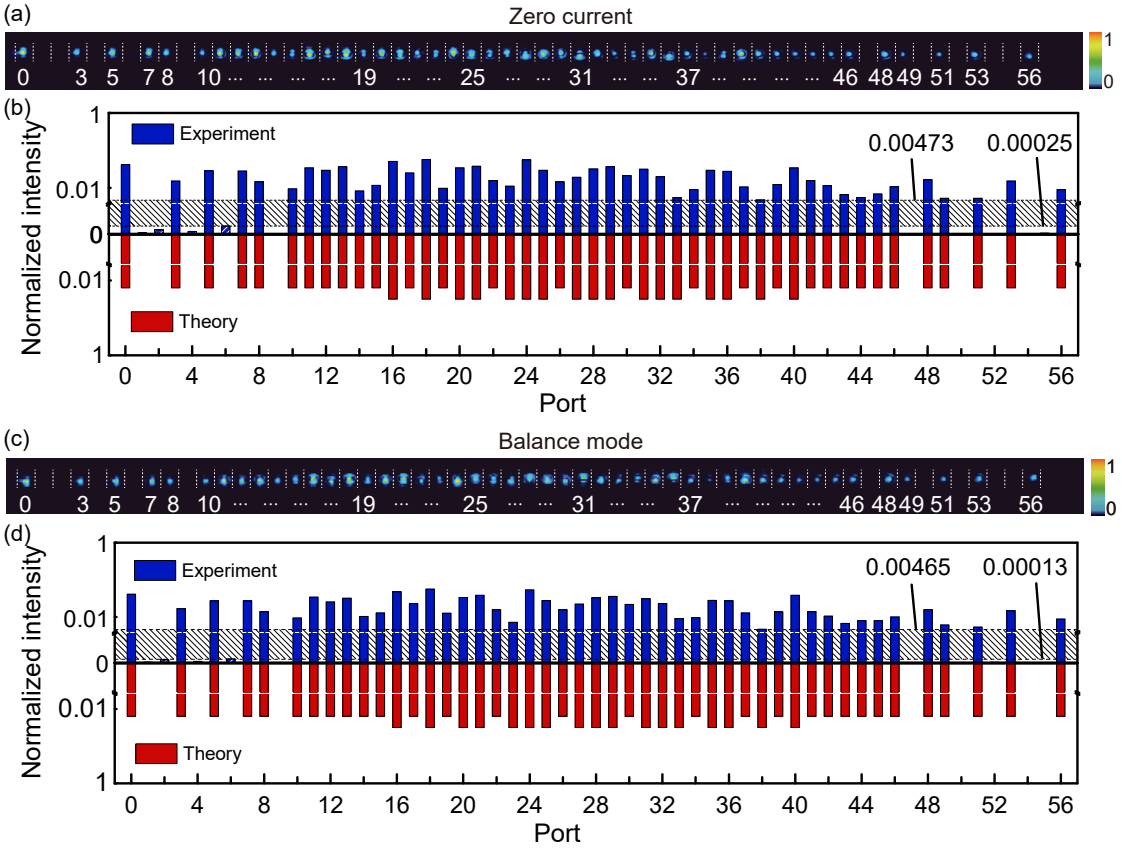

Fig S9 The computing results of the case $\{3, 5, 7, 11, 13, 17\}$ under different conditions. (**a**) The experimental read-out and (**b**) intensity distribution when zero current applied to VS junction 1 (i.e., zero dissipated power). (**c**) The experimental read-out and (**d**) intensity distribution when VS junction 1 is set to balance mode (i.e., nonzero dissipated power).

As a contrast, we deliberately set VS junction 1 to balance mode (the dissipated power is 113.6 mw) and keep other settings of the photonic processor unchanged. Obviously, if the thermal crosstalk is negligible, the working mode of VS junction 1 does not influence the computing results. Otherwise, the computing results obtained on the new conditions should deviate from the original

results. As presented in Figs. S9(c)-S9(d), the experimental computing results are highly similar to the previous case. The similarity is up to 99.86%, which is calculated by

$$\theta = \sum_i \sqrt{I_i^0 I_i} \tag{S2}$$

where I_i^0 (I_i) is the normalized intensity at output port i when zero (non-zero) current is applied to VS junction 1. The result strongly confirms the negligibility of the thermal crosstalk in our experiments.

10 Signal-to-noise ratio

The singal-to-noise ratio (SNR) can be written as

$$\begin{aligned} SNR &= 10log_{10}(Sig/Noi) \\ &= -10log_{10}(In/Sig) + 10log_{10}(In/Noi) \end{aligned} \tag{S3}$$

where Sig is the power of the weakest output signal, Noi is the environmental noise and In is the input power [Ref. 28]. In the photonic processor, the weakest output signal is supposed to go through the longest path. Therefore, the first term has a form of

$$F = -10log_{10}(In/Sig) = C_1 N + C_2 q + C_3. \tag{S4}$$

Based on the parameters of the photonic processor, including propagation loss, bending loss, splitting ratio, etc., we have $C_1 = -3.7804$ in the case of fixed split junction ($C_1 = -4.2024$ in the case of variable split junctions), $C_2 = -0.0165$ and $C_3 = -2.8460$.

The second term, $10log_{10}(In/Noi)$, is independent on problem size N and determines the upper bound of the SNR. For silicon detectors [Ref. 58], the dark count rate can be down to 100 Hz in the regime of 40MHz count rate. In this case, the noise in one-shot detection is down to 0.0000025. With an input power of 1 nJ, 1 μJ and 1 mJ, the estimated SNRs maintain at a reasonable level even for a relatively large-sized problem as presented in Fig. S10.

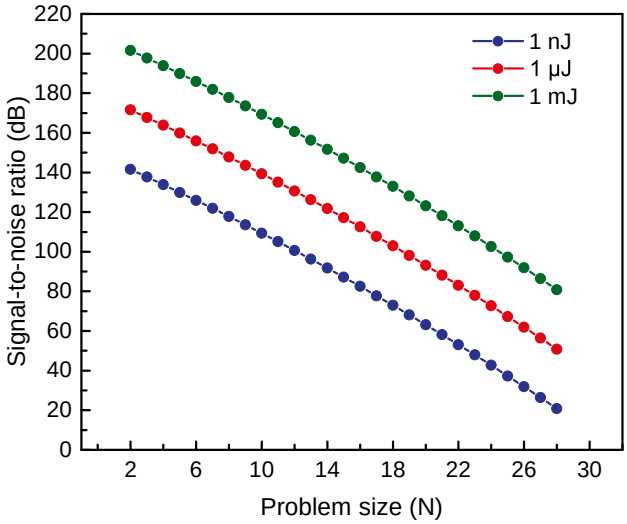

Fig S10 Signal-to-noise ratio. The estimated signal-to-noise ratio of the photonic processor under the condition of an input power of 1 nJ, 1 μJ and 1 mJ, respectively.

11 Related work

(1) Solving the SSP with light

Oltean and Muntean theoretically proposed an optical solution for solving the SSP based on optical fiber system and delayed light rays. As depicted in Fig. S11, light is divided into two portions at a red node (except the destination). The two portions are then forced to pass through two different arcs (i.e., optical fibers). Given a set of positive numbers $A = \{a_1, a_2, \ldots, a_N\}$, one of the optical fibers has a constant length of k, the other has a length of $a_i + k$, where a_i is the number in the set and k is deliberately added. The incident light is finally divided into 2^N individual portions to

traverse every possible path from the start to the destination, therefore generating every possible subset. We can see that, in Oltean and Muntean's proposal, the parallelism of light is used, which is similar to our experiments. Nowadays, commercial detectors are able to detect an optical signal down to single-photon level ($\sim 10^{-19}$J) [Ref. 58]. This enables us to treat single photons as individual information carriers, making it easy to obtain a vast number of individual information carriers with a commercial laser.

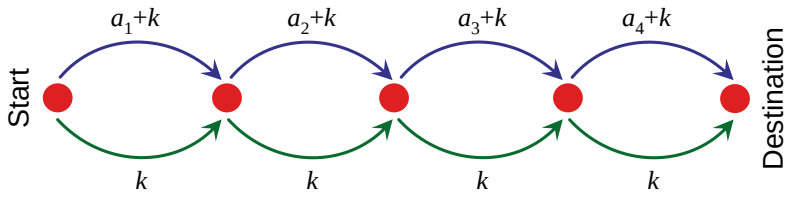

Fig S11 Optical solution based on delayed light rays. Red circle: nodes. Blue and green lines: arcs.

In terms of encoding, they encode the subset sums into the delay time of light rays. Ideally, light rays encoding different subset sums will arrive at the destination node at different moments. The solution to the problem can be obtained by detecting whether there is a signal at particular moment. As the authors point out, the difficulty of this proposal lies in satisfying the following constraint: assuming the signal encoding the solution to the subset sum problem has a delay of B, any signals which do not encode the solution can't have the same delay. To address this, the authors proposed a clever and useful scheme. In this scheme, the lengths of the optical fibers must be integer multiples of the length that induces a defined minimum delay, which effectively guarantees that the constraint is met.

In our approach, we encode the subset sums into the spatial position of light. The position of the output optical signals is indicated by the corresponding output port numbers (as shown in Fig. 1(b) in the main text), which provides a straightforward way to make distinction between different output signals. Despite the differences and similarities, the two approaches both show that light

can be an excellent candidate to deal with complicated computation. It should be emphasized that we have implemented a photonic processor comprising 1449 integrated optical modules, which, to the best of our knowledge, is the largest integrated photonic processor for solving the subset sum problems. Based on the fabricated photonic processor, we experimentally confirm that the photonic approach can solve the subset sum problem with high accuracy, as shown in Figs. 2-3 in the main text. Moreover, our photonic processor has genuinely surpassed representative electronic processors launched in recent years, such as Intel Core i7-11370H and i7-1160G7, in computation time (as presented in Fig. 4 in the main text).

(2) Reconfigurability

Reconfigurability is a critical foundation for a NP-complete problem solver to step towards practical applications. Oltean and Muntean theoretically proposed two ways to realize reconfigurability in the framework of delayed signal. The first one is to make it possible to enable/disable the arcs between the nodes (see Fig. S11 for schematic diagram). The second one is to make the delay lines programmable. Once the two requirements are fully met, the solver will be highly reconfigurable and could solve much more NP-complete problems.

Our reconfigurable photonic processor is not based on delayed signals. Nevertheless, we have truly endowed the photonic processor with reconfigurability through a method somehow equivalent to "enable/disable the arcs". As presented in Fig. 1(g) in the main text, we offer two paths to program the photonics processor. Firstly, we can remove the first $i-1$ elements by choosing the i_{th} entry as the input. Secondly, we are able to delete or keep the element X_j by appropriately tunning the working modes of the j_{th} row of variable split junctions. The operation of delete an element or not, to some extent, is similar to disable or enable the arc that induces a delay. It should

be noticed that our reconfigurable architecture is not limited to solving NP-complete problems, but could be used in more applications, such as optical neural networks and photonic quantum memristors (see Supplementary Section 14).

12 Phase stability and interference visibility

Integrated photonics has offered an excellent platform to realize monolithic optical system. Compared with bulk optical systems, integrated photonic chips show inherent strengths in stability, compactness and scalability. Besides the contribution from monolithic integration, we have also made specific efforts in technologies to ensure highly reliable fabrication. As introduced in the main text, our femtosecond laser direct writing system is equipped with a laser beam-pointing stabilizer, which can fix the pointing angle at lower than 0.5 μrad. In addition, the position deviation of the air-bearing three-dimensional translation stages is down to ± 0.05 μm, which is many orders of magnitude smaller than the size of a single interferometer (usually at a level of millimeters). It is worth stressing that the stability and high precision of our fabrication is verified even in the context of quantum information which is more sensitive to imperfectness. For example, we have successfully prepared 128 identical quantum sources on a single silica chip using this femtosecond laser direct writing system [Ref. 59]. The stable and highly precise fabrication lays a crucial foundation for the excellent phase stability and interference visibility as we show below.

(1) Phase stability

A light beam can be divided into two portions at fixed split junctions or those variable split junctions working at balanced mode. An effective interferometer of larger size could be generated as the split light propagates. An example in shown Fig. S12. As we can see, the incident light (parent)

is split and two of its offspring light beams meet at a second split junction and interfere with each other. On this occasion, an effective larger interferometer is formed. The two beam splitters of the interferometer are marked by red and green dashed lines, respectively. The two interferometer arms are indicated by the paths highlighted in pink and blue, respectively. It should be noted that we do not highlight all the possible propagation paths of the injected light.

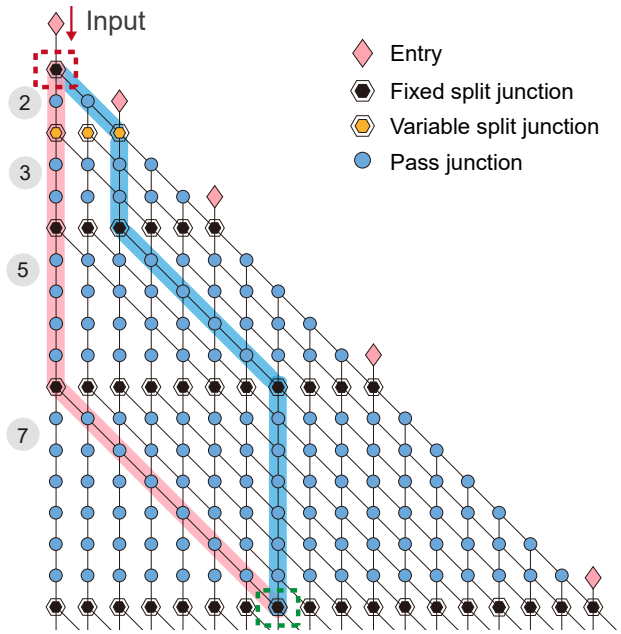

Fig S12 An example of an effective interferometer.

The phase stability of an interferometer is related to its arm length difference. In the following, we will give a general expression of the arm length difference of an effective interferometer that could be formed in our photonic processor. As introduced in the main text, the propagation path of light indicates whether the corresponding elements is included. For an effective interferometer, its two arms correspond to two propagation paths. Assume that the number of elements which are included by path 1 (path 2) but excluded by path 2 (path 1) is M_1 (M_2). As the two paths have the same starting and ending split junctions, the sum of the M_1 elements is equal to the sum of the M_2 elements.

Based on the above facts and the architecture of our photonic processor, the absolute value of the arm length difference is written as

$$|\Delta L| = |\gamma\left(M_1 - M_2\right)| \leq |\gamma| \times \left(|M_1| + |M_2|\right), \tag{S5}$$

where $\gamma = -4.1522 \times 10^{-4}$ mm is a constant coefficient determined by the actual geometrical parameters of the photonic processor. As M_1 and M_2 are non-negative, we then have

$$|\Delta L| \leq |\gamma| \times \left(M_1 + M_2\right) \leq |\gamma| \times N, \tag{S6}$$

where N is the total number of elements in the set. Based on equation (S6), even when $N = 100$, the upper bound of the arm length difference keeps at a very low level, which is about 0.0415 mm. According to the thermal expansion coefficient of glass $0.5 \times 10^{-6}/K$, the fluctuation of arm length difference corresponding to a variation of 2 K at temperature (considerably large variation for a laboratory) is about 4.15×10^{-2} nm, which is several orders of magnitude smaller than the wavelength of the incident light (808 nm). Therefore, the phase fluctuation of our photonic processor is completely ignorable.

(2) Interference visibility

For an interferometer, unbalanced beam splitters can result in a decrease of interference visibility. According to the coupled mode theory, the splitting ratio of a directional coupler, which acts as a beam splitter in our work, is $cos^2(C \times Z) : sin^2(C \times Z)$, where C is the evanescent coupling strength and Z is the coupling length. When $C \times Z = \pi/4$, a splitting ratio of 50:50 is obtained. Due to the imperfectness of fabrication, there could be a deviation of both C and Z from the ideal

case, thus resulting in a deviation of reflectivity $\eta = cos^2(C \times Z)$. The deviation of η is written as

$$d\eta = d\left(\cos^2(C \times Z)\right) = -2 \times \cos(C \times Z) \times \sin(C \times Z) \times (Z \times dC + C \times dZ), \qquad (S7)$$

where dC and dZ are the differentials of C and Z, respectively. We then have

$$d\eta|_{C \times Z = \pi/4} = -\left(\frac{\pi}{4 \times C} \times dC + C \times dZ\right) \qquad (S8)$$

It should be noted that the coupling strength C is a function of waveguide spacing X, as shown in Fig. S13. Based on the experimental data measured recently, we have $C(X) = 6.52997 \times \exp(-0.25611 \times X)$. Taking $X = 10\mu\text{m}$ as an example, we obtain $C(10) \approx 0.50424$ and the differential dC is expressed by

$$dC = -0.25611 \times 6.52997 \times \exp(-0.25611 \times X) \times dX, \qquad (S9)$$

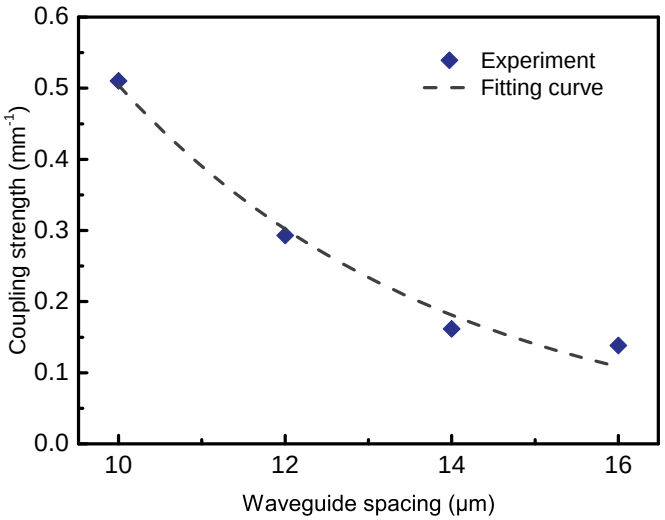

Fig S13 Coupling strength versus waveguide spacing.

As introduced above, the position deviation of our fabrication system is $\pm 0.05\mu\text{m}$. Therefore,

we have $dX = \pm 0.05\mu\text{m}$ and $dZ = \pm 0.05\mu\text{m}$. Substitute dX and $X = 10\mu\text{m}$ into equation (S9) to obtain dC. Then, substitute dC, $C(10)$ and dZ into equation (S8). Finally, we obtain that the deviation of reflectivity $d\eta|_{C\times Z=\pi/4,\quad X=10\mu m}$ is in the range of [-0.0101,0.0101]. For $d\eta = -0.0101$, the splitting ratio becomes 48.99:51.01. In this case, the interference visibility of the basic interferometers (i.e., the variable split junctions) is calculated by $V = \frac{2\sqrt{I_1 I_2}}{I_1+I_2}$, where I_1 and I_2 denote the intensities of the two beams that interfere with each other. Therefore, the interference visibility is equal to $2 \times \sqrt{48.99 \times 51.01}/(48.99 + 51.01) \approx 0.9998$. In a worse case, where the splitting ratio is 45:55, the interference visibility still keeps at a high level, which is about 0.995. In addition, when it comes to an effective interferometer composed of two variable split junctions, the interference visibility is 1, given the fact that the variable split junctions in principle can act as a balanced beam splitter.

13 High-density integration of phase shifters

High-density integration of phase shifters on femtosecond-laser-written silica photonic chips is more challenging than silicon photonic chips. The main difficulties include: (1) Phase shifters on silica chips are not separated by isolation trench. As the thermal conductivity of glass ($\sim 10^0 W/m/K$) is much higher than air ($\sim 10^{-2} W/m/K$), larger physical distance is required to reduce thermal crosstalk compared with silicon chip. (2) Femtosecond-laser-written silica waveguides are always buried inside silica chips, leading to indirect heating from the phase shifters on the chip surface. The indirect contact lowers the heating efficiency. Therefore, it is more difficult to decrease the size of the phase shifters.

However, there are some possible methods to cope with the challenge. (1) Fabricating isolation trench in femtosecond-laser-written silica photonic chips. Recently, researchers have reported

successful fabrication of isolation trench through water-assisted laser ablation method, which is compatible with femtosecond laser direct writing system [Ref. 36]. They succeeded to prepare trenches (a width of 60 μm, a depth of 300 μm and a length of a few millimeters) on a silica photonic circuit where the pitch of the target waveguides is 160 μm. Though the pitch of the target waveguides in our case is 40 μm (see Fig. S1), which is much smaller than 160 μm, the advancement in trench fabrication provides a possible route to integrate more phase shifters on our photonic chips.

(2) Writing waveguides at a shallower depth. As introduced in the main text, we write the target waveguides (i.e., the waveguides with phase shifters deposited) at a shallow depth of 55 μm to improve the heating efficiency. A higher heating efficiency can be acquired with a shallower embedment. Generally, if a waveguide is written too close to the chip surface, it is hard to form a single-mode waveguide with strong confinement. However, it is possible to realize strongly-confined single-mode waveguides at a depth of 30 μm by employing multi-scan laser writing techniques and thermal annealing treatment [Ref. 36]. Moreover, near-surface single-mode waveguides with high index contrast can be realized by putting a glass cover slide on the top surface of the glass sample to be fabricated [Ref. 37].

14 Other applications of the reconfigurable photonic computing architecture

The proposed reconfigurable photonic computing architecture is not limited to solving the subset sum problems. We show that it can be used in implementing optical convolutional neural networks and photonic quantum memristors.

(1) Optical convolutional neural network

As displayed in Fig. S14, the network made of interferometers is one of the typical structures used to implement optical convolution operation [Ref. 56]. Elements in the convolution kernel are encoded by the first column of interferometers while elements in the input matrix to be processed are encoded by the second column of interferometers. A summation of the intensities at the output channels generates the ultimate outcome. We can configure our photonic computing architecture to be the same structure. For convenience, we use a small network to illustrate the implementation. As presented in Fig. S15, the second entry acts as the input, the split junctions encircled by red dashed lines are used to split the incident light into four portions. Besides, the split junctions marked by green dashed lines are responsible for encoding the convolution kernel elements while those marked by black dashed lines are utilized to encode the matrix elements. A summation of the optical intensities at output ports 2, 5, 7 and 10 generates the outcome. It should be noted that, during subsequent propagation, the remaining split junctions which are located in the path towards the above output ports should be properly set to fully maintain the current propagation direction, like pass junctions.

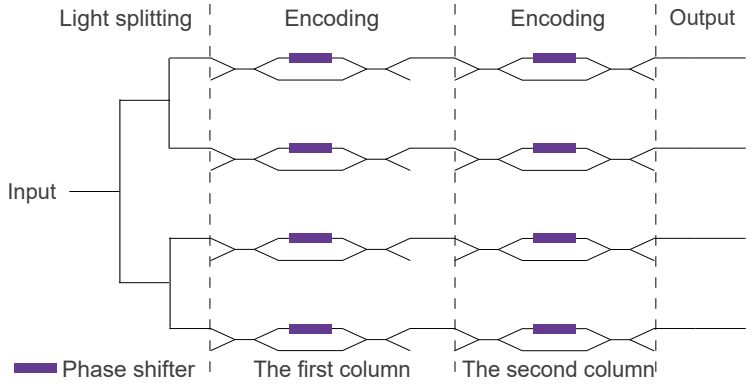

Fig S14 A typical structure used for optical convolution operation.

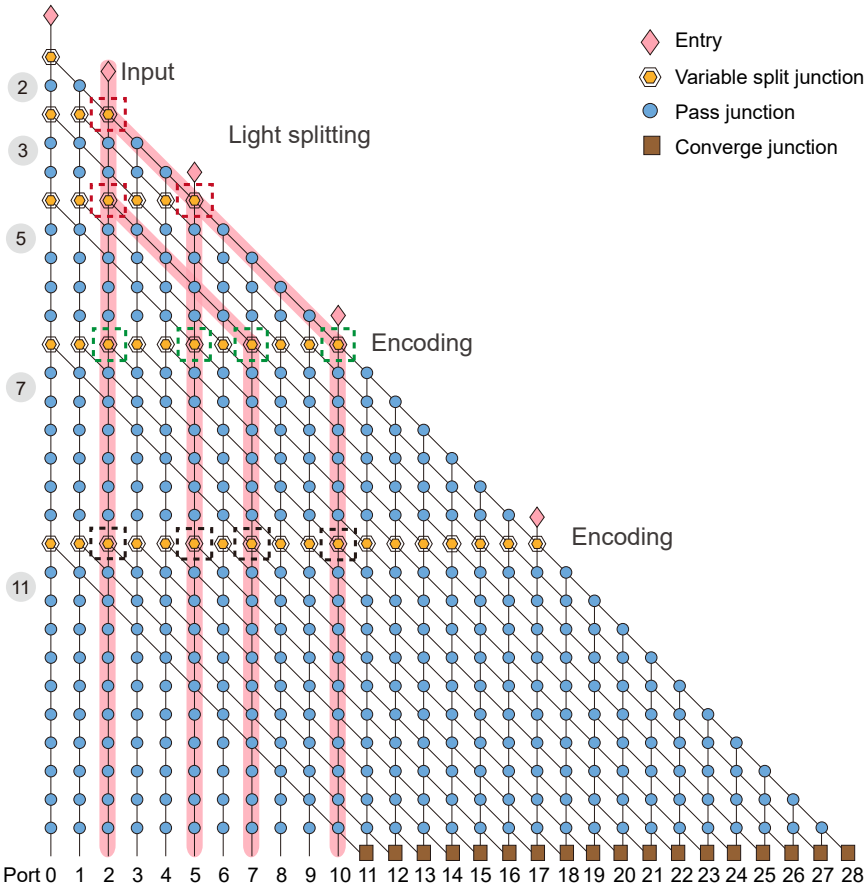

Fig S15 The configuration for implementing optical convolution operation. The path highlighted in ping denotes the propagation of light for the convolution operation.

(2) Photonic quantum memristor

As displayed in Fig. S16, the network made of cascaded interferometers is the structure used for a photonic quantum memristor [Ref. 57], where single photons are injected. We can also implement the same structure by reconfiguring our photonic computing architecture. As exhibited in Fig. S17, the first entry acts as the input, the split junction encircled by red dashed lines is used for the state preparation and the one marked by green dashed lines play a role of the memristor. Also, the split junction indicated by black dashed lines is employed to carry out the state tomography. Port 0 is the output channel connected to the controller, and ports 5 and 12 correspond to the other two outputs. It should be noted that the remaining split junctions which are located in the paths towards

the above ports should be appropriately set in order to realize the propagation indicated by the path in pink. For example, in the last row of split junctions, three of them are located in the path. The left and the middle ones should be set to maintain the previous propagation directions while the right one should be set to change the propagation direction.

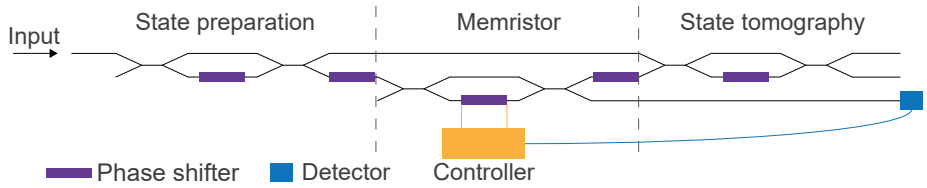

Fig S16 The structure used for a photonic quantum memristor.

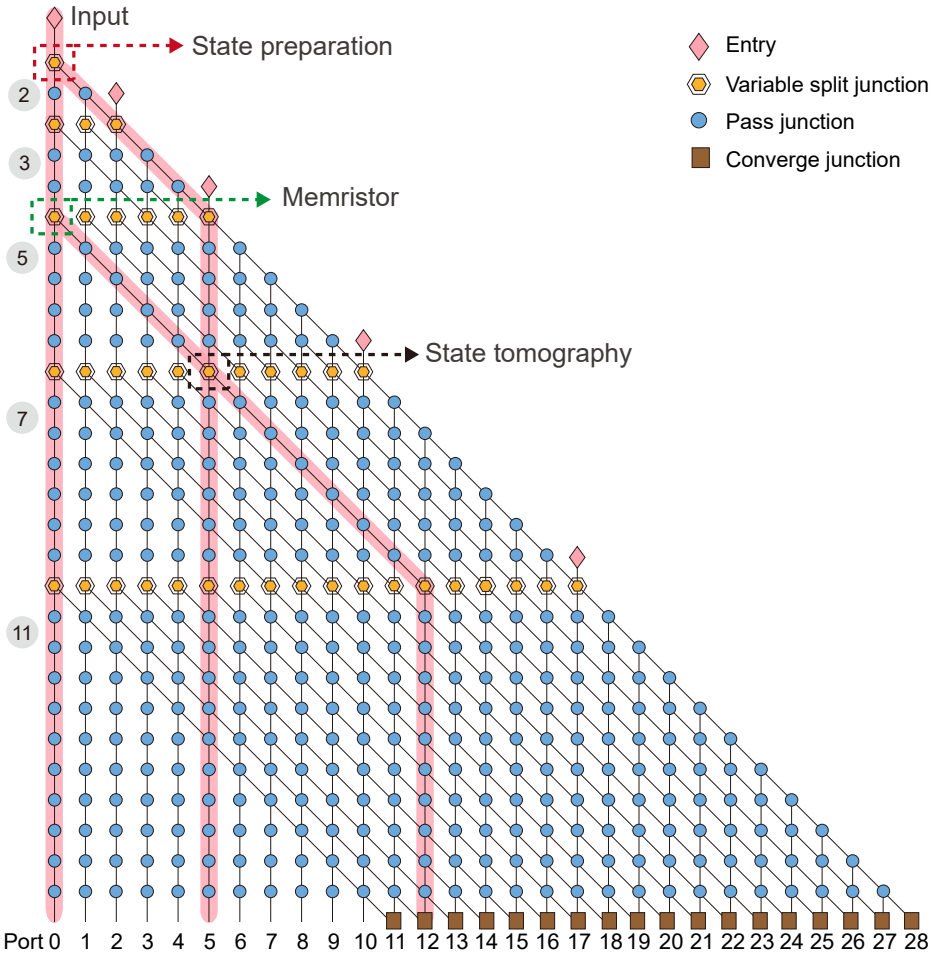

Fig S17 The configuration for implement a photonic quantum memristor

15 Physical size

(1) Optimizing the intersection angles

As indicated by the green arrows in Fig. S18, the intersection angle ρ in the current photonic processor is fixed at 2.78 degrees. However, as the element value increases, there is sufficient space to realize larger angles. Obviously, increasing intersection angle can shorten the length (i.e., the size in the x direction) of the photonic processor. We optimize the intersection angles corresponding to different elements in the set, using the same optimization strategy. In this case, the physical size of the photonic processor can be greatly reduced as displayed in Fig. 4(c) in the main text.

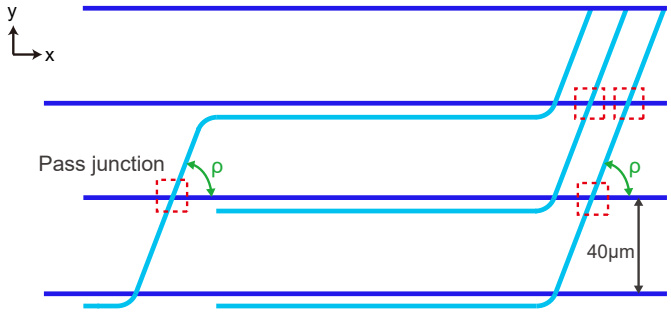

Fig S18 Local waveguide network in the x-y view. The two waveguides in the pass junctions (marked by red dashed lines) have a fixed intersection angle ρ, as indicated by the green arrows.

(2) Mapping a large-sized set to a silica glass chip

As introduced in the main text, for a silica glass chip with a length of 250 mm and a width of 110 mm, the size of the set that could be mapped to the chip is up to $N = 30$. As depicted in Fig. S19, the silica glass chip is divided into three regions. The output interface of region 1 is connected to the input interface of region 2 through a low-loss planar photonic integrated circuit (PPIC) such as silicon nitride. Similarly, the output interface of region 2 is connected to the input interface of

region 3. Coupling between planar photonic integrated circuits and silica waveguides is technically possible [Ref. 60-61]. Moreover, at $N = 30$, the photonic processor is able to surpass state-of-the-art supercomputers in computing time. With an input power of 1 mJ and employing single-photon detectors [Ref. 58], the signal-to-noise ratio at $N = 30$ can be maintained at a considerably high level ($\sim$ 57 dB), which is tolerant of the insertion loss brought by the PPICs.

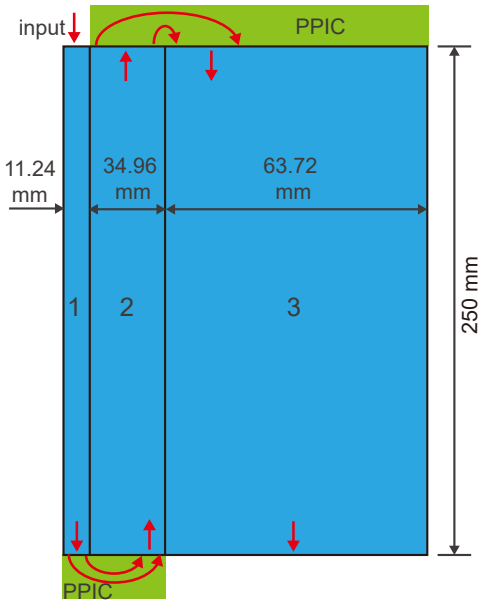

Fig S19 A sketch of the silica glass chip. PPIC: planar photonic integrated circuit.

16 Compare with dynamic programming algorithm

As introduced in the main text, our photonic processor can generate all possible subset sums at a time, which, to some extent, is equivalent to simultaneously solving a series of SSP instances whose target T is different. This capability allows us to apply the photonic processor in scenarios requiring the solution of a large number of SSP instances, such as workload balancing problems. For a fair comparison, we compare our photonic processor with the dynamic programming algorithm which can also provide all subset sums (i.e., search the entire solution space). As presented by Bellman [Ref. 62], the dynamic programming algorithm runs in $O(N^2h)$ if all numbers in the

set are bounded by a fixed constant h. Under the same conditions, our photonic processor has a runtime of $O(N + Nh)$, which is linear to N for constant h.